optics

MDPI

Article

Experimental Demonstration of Terahertz-Wave Signal Generation for 6G Communication Systems

Yazan Alkhlefat [1,*], Amr M. Ragheb [2], Maged A. Esmail [3], Sevia M. Idrus [1], Farabi M. Iqbal [1] and Saleh A. Alshebeili [2]

[1] Department of Electrical Engineering, Universiti Teknologi Malaysia, Johor Bahru 81310, Malaysia; sevia@utm.my (S.M.I.); alfarabi@utm.my (F.M.I.)
[2] Department of Electrical Engineering, College of Engineering, King Saud University, Riyadh 12372, Saudi Arabia; amrragheb79@gmail.com (A.M.R.); dsaleh@ksu.edu.sa (S.A.A.)
[3] Department of Communications and Networks Engineering and Smart Systems Engineering Lab, Prince Sultan University, Riyadh 11586, Saudi Arabia; mesmail@psu.edu.sa
* Correspondence: amyazan1988@graduate.utm.my

Abstract

Terahertz (THz) frequencies, spanning from 0.1 to 1 THz, are poised to play a pivotal role in the development of future 6G wireless communication systems. These systems aim to utilize photonic technologies to enable ultra-high data rates—on the order of terabits per second—while maintaining low latency and high efficiency. In this work, we present a novel photonic method for generating sub-THz vector signals within the THz band, employing a semiconductor optical amplifier (SOA) and phase modulator (PM) to create an optical frequency comb, combined with in-phase and quadrature (IQ) modulation techniques. We demonstrate, both through simulation and experimental setup, the generation and successful transmission of a 0.1 THz vector. The process involves driving the PM with a 12.5 GHz radio frequency signal to produce the optical comb; then, heterodyne beating in a uni-traveling carrier photodiode (UTC-PD) generates the 0.1 THz radio frequency signal. This signal is transmitted over distances of up to 30 km using single-mode fiber. The resulting 0.1 THz electrical vector signal, modulated with quadrature phase shift keying (QPSK), achieves a bit error ratio (BER) below the hard-decision forward error correction (HD-FEC) threshold of 3.8×10^{-3}. To the best of our knowledge, this is the first experimental demonstration of a 0.1 THz photonic vector THz wave based on an SOA and a simple PM-driven optical frequency comb.

Keywords: 6G; optical frequency comb generator; photonic technologies; THz-wave signal generation; uni-traveling carrier photodiode (UTC-PD)

check for updates

Academic Editor: Paulo Pereira Monteiro

Received: 3 April 2025
Revised: 26 June 2025
Accepted: 1 July 2025
Published: 28 July 2025

Citation: Alkhlefat, Y.; Ragheb, A.M.; Esmail, M.A.; Idrus, S.M.; Iqbal, F.M.; Alshebeili, S.A. Experimental Demonstration of Terahertz-Wave Signal Generation for 6G Communication Systems. *Optics* **2025**, *6*, 34. https://doi.org/10.3390/opt6030034

Copyright: © 2025 by the authors. Licensee MDPI, Basel, Switzerland. This article is an open access article distributed under the terms and conditions of the Creative Commons Attribution (CC BY) license (https://creativecommons.org/licenses/by/4.0/).

1. Introduction

Recently, the data traffic in different communication systems is increasing rapidly, so it is imperative to develop new spectrum resources for next-generation networks (e.g., 6G). To meet the requirements of 6G and its applications, such as the Internet of Things (IoT), space communication networks, wireless data centers, precise telemedicine control, and holographic communication [1,2], THz band communications have attracted considerable attention and are considered as a key technology in pillar for 6G networks [3]. THz frequency range closes the gap between the millimeter wave (mmWave) and the optical frequency band. In the comparison between THz communication and mmWave communi-

cation, THz communications own more spectrum resources that offer higher data rates in the range of hundreds of gigabits per second (Gbps) to some terabit per second (Tbps) [4].

The THz frequency band has the potential to enhance communication performance in challenging propagation environments by leveraging reflected paths. As a result, THz technology is seen as the most promising option for 6G networks [5]. Research has explored the electromagnetic spectrum from 0.1 THz to 10 THz, corresponding to wavelengths ranging from 3 mm to 30 µm, known as the low-THz band [6–9]. The equipment requirements for the low-THz band are less demanding than those for higher THz frequencies, yet it retains many characteristics of THz signals, making low-THz a prominent area of research [9].

High-frequency electromagnetic radiation can be understood as either particle processed through photonic devices (optical medium) or as waves managed by electronic devices (mmWave medium) [10]. Consequently, the design of modern photonic and electronic THz transceivers has been enhanced to enable efficient signal generation, modulation, and radiation [11–14]. In this context, metamaterials are a key solution for enhancing performance and enabling applications in 5G and 6G communication systems, while dielectric materials play a vital role in designing electronic devices such as antennas and sensors for future IoT applications, as indicated in [15] and [16], respectively.

The photonic solutions can be utilized to achieve higher carrier frequencies, making them essential for applications that require high data rates, although they tend to have lower output power and integration levels [10]. These photonic approaches employ various technologies, such as quantum cascade lasers [17], uni-travelling carrier photodiodes [18], photoconductive antennas [19], and optical down-conversion systems [20].

Additionally, advancements in the understanding of light's topological phase are being harnessed to enable robust transmission of THz topological valleys through multi-sharp curves in integrated THz waveguides [21].

Figure 1 categorizes the different THz generation techniques. Given our focus on photonic solutions for THz generation, we will delve deeper into the key technologies utilized in this area including uni-travelling carrier photodiodes (UTC-PDs) and OFCG. UTC-PDs are known for their high-speed performance, which is essential in our THz signal generation experiments where, in our research, we utilize UTC-PDs to achieve efficient signal modulation and enhance the overall performance of our THz systems. Next, the UTC-PD is introduced as it directly influences the quality and feasibility of our THz signal generation methods.

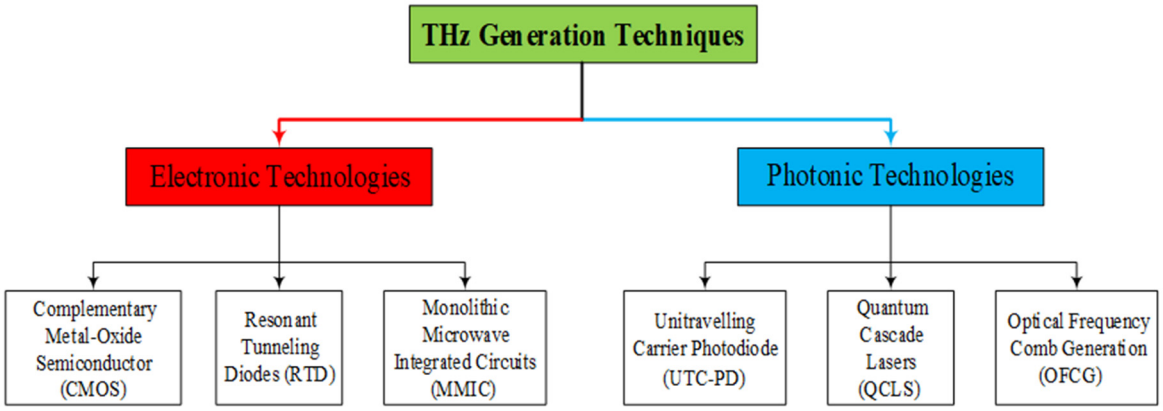


Figure 1. Terahertz generation techniques classification.

1.1. Uni-Travelling Carrier Photodiode (UTC-PD)

The rapid advancement of photonics technology is significantly enhancing signal processing speeds within related systems. Devices such as photodiodes offer the advantage

of both high saturation output and high speed, which contribute to the development and improvement of large-capacity communication systems. By combining an optical amplifier with a high saturation power photodiode, it is possible to extend bandwidth, eliminate the need for post-amplification electronics, and simplify the receiver configuration [22]. UTC-PDs are particularly promising for these applications due to their unique operational mode [23].

UTC-PDs are a type of pin-junction photodiode that utilizes selected electrons as active carriers. Their structure features a thin *p*-type absorber where electrons are generated as minority carriers, which then spread or accelerate towards the collector. The high velocity of electrons traveling through the depleted collector allows UTC-PDs to outperform conventional pin photodiodes in terms of photo response [24].

These photodiodes are reported to have a bandwidth of 150 GHz [25] and exhibit a high saturation output current due to the reduced space charge effects in the depletion layer caused by the rapid electron velocities [26]. Since their introduction in 1997 [27], UTC-PDs have been employed as photo-mixer chips, operating at frequencies ranging from 75 to 170 GHz. In 2003, the integration of UTC-PDs with planar antennas was demonstrated, achieving operation frequencies exceeding 1 THz [28]. Furthermore, integrated antennas in UTC photo-mixers have been shown to operate at frequencies above 2 THz [29]. UTC-PDs also utilize traveling-wave designs, which provide a slower frequency response roll-off and facilitate better integration. In [30], UTC-PDs were reported to produce output powers of 24 μW at 914 GHz and 148 μW at 457 GHz. Additionally, a THz wireless link achieving 160 Gbps was realized using a single UTC-PD in the 300–500 GHz range, as noted in [31].

1.2. Optical Frequency Comb Generator (OFCG)

The optical frequency comb (OFC) generation technique has garnered significant interest among researchers due to its various advantages, including the ability to transmit high data rates at a low cost. In optical networks, OFC is commonly used as a multi-wavelength source at the optical line termination (OLT) side, facilitating optical communication systems that utilize optical time division multiplexing (TDM), dense wavelength division multiplexing (DWDM), and quadrature amplitude modulation (QAM) [32–37]. Additionally, OFC is a compelling area of study because of its relevance in optical wave generation, optical communications, and optical frequency meteorology [38–40]. For effective use, the generated OFC should feature variable frequency spacing, a high tone-to-noise ratio (TNR), excellent flatness, and the potential to reduce OLT costs by replacing laser sources and other system components [41].

In recent years, numerous techniques and methods for OFC generation have been proposed [38,42–47]. The most commonly employed methods include recirculating frequency shifting (RFS) loops, mode-locked lasers (MLL), and nonlinear effects in highly nonlinear media. The RFS loop technique is noted for its ability to generate a larger number of comb lines; however, its complexity requires additional components, making it less manageable. For example, the structure of the proposed dual RFS loops in [48] is intricate, leading to instability in the generated comb lines and difficulties in maintenance. This technique also exhibits a maximum power deviation exceeding 10 dB between the resulting comb lines in the generated spectrum. The MLL approach allows for high bandwidth in the produced OFCs, but controlling the OFC generator presents challenges. Lastly, the method leveraging nonlinear effects in highly nonlinear media often results in issues with comb line flatness and lacks continuous tunability for the generated spectrum.

A widely studied and intriguing method for generating OFCs involves optical modulation. This method can be divided into two main components: the first component includes intensity modulators (IMs) [49–51], parallel or cascaded IMs [41,52], phase modulators

(PMs) [46,53], and polarization modulators [54,55]. The second component involves hybrid modulators, such as cascaded combinations of IMs and PMs [56]. This technique is favored for its simplicity and cost-effectiveness, making it a popular choice for generating OFC lines. However, it may sometimes require high driving RF voltages.

In conclusion, among the various techniques discussed for OFC generation, the most commonly utilized method is based on IMs due to their high quality and flexibility. IMs are typically driven by radio frequency (RF) sources alongside light sources. The RF driving frequency is tunable and can be adjusted to achieve an ultra-flat OFC spectrum.

1.3. Paper's Contributions

This paper introduces a novel approach to generating photonic vector THz-wave signals in the THz frequency range. By integrating a Mach–Zehnder modulator (MZM) with a semiconductor optical amplifier (SOA) to create an optical frequency comb, and employing an IQ modulator for signal modulation, we demonstrate the effective generation of QPSK vector THz-wave signals. Our methodology includes simulations and laboratory experiments that showcase the transmission of these signals over long distances.

In our experimental setup, a 4 Gbps QPSK-modulated baseband signal is applied to an IQ modulator, while a 12.5 GHz radio frequency source drives a Mach–Zehnder modulator (MZM) to generate an optical frequency comb. The optical signals are then mixed in a UTC-PD through heterodyne detection, producing a 0.1 THz radio frequency signal. This THz wave is transmitted over a 35 km length of single-mode fiber. The resulting 0.1 THz electrical vector signal, encoded with QPSK modulation, achieves a bit error rate (BER) below the hard-decision forward error correction (HD-FEC) limit of 3.8×10^{-3}.

UTC-PDs, known for their high-speed performance, play a crucial role in our THz signal generation experiments. Their efficiency in signal modulation enhances the overall performance of our THz systems, directly impacting the quality and feasibility of our methods.

Our innovative approach offers several advantages over existing systems, particularly those using intensity, phase, and polarization modulators. These advantages include:

Wider OFC Line Generation: The nonlinear effects, such as four-wave mixing (FWM) enabled by the SOA, result in a greater number of OFC lines, thereby extending the range of the generated THz signal.

Enhanced Signal Quality: Our system benefits from the optical frequency comb, providing improved clarity and coherence, which enhances overall performance.

Flexibility in Modulation: The IQ modulator allows for superior manipulation of both phase and amplitude, enabling more complex signal encoding compared to traditional modulators.

Improved Efficiency: The combination of the MZM and SOA optimizes power consumption and bandwidth efficiency, which is essential for high-frequency THz applications.

In summary, our method stands out due to these enhancements, leading to better performance in terms of signal fidelity and operational versatility. This contribution is significant, opening new avenues for sensing and communication applications within the THz frequency range.

Table 1 offers a concise overview of THz generation techniques, outlining the methods used and their respective frequencies, along with brief remarks on each.

Table 1. Closely Related Works in THz Generation.

Generation Technique	Modulation Format	Freq Separation in RF Source (GHz)	Generated Frequency (THz)	Method of Conduct	Remarks	Reference
Tunable optoelectronic oscillator (OEO)	QPSK/16 QAM	17.33	0.101 and 0.242	Experimental	The generated THz signals depend on the OEO stability, which makes the implementation critical.	[57]
Optical frequency comb using two-phase modulators	QPSK/16 QAM	25	0.4	Simulation	This paper utilized two cascaded phase modulators, leading to expensive implementation.	[58]
Single-section chirped multiple InAs/InP quantum-dot (QD) mode-locked laser (MLL)	--	--	1–2.9	Experimental	The programmable optical filter can work only in the C-band, so the longer wavelength modes cannot be extracted.	[59]
Optical feedback mode-lock laser diode	64-QAM	--	0.042–0.377	Experimental	Focusing on reducing the optical linewidth to use higher-order modulation.	[60]
Integrated dual-distributed feedback (DFB) laser	16QAM-OFDM	9.951	0.408	Experimental	This paper used a monolithically integrated (DFB) laser chip attached to a (UTC-PD) with a THz antenna	[61]
OFCG using phase modulator with SOA and UTC-PD	QPSK	12.5	0.1	Simulation/ experimental	This work presents a simple and efficient method for generating THz signals.	This work

2. Simulation Model for THz Generation

Figure 2 illustrates the core principle behind the terahertz (THz) wave generation technique employed in our system, which involves three main stages: the transmitter, the wavelength selection switch (WSS), and IQ modulation, ultimately leading to the receiver.

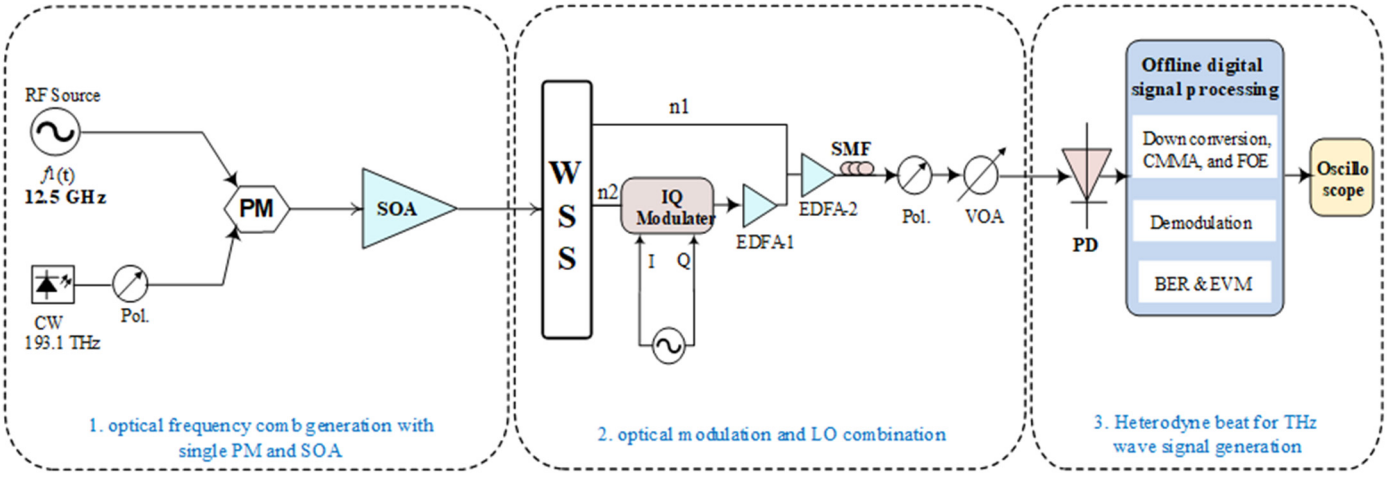


Figure 2. Simulation model for THz generation based on optical frequency comb by using single PM and SOA.

At the heart of the transmitter is the generation of multiple OFC lines, which serve as the optical carriers for THz generation. This process begins with a continuous wave (CW) laser, which provides a stable optical carrier. To produce a broad spectrum of frequencies, a radio frequency (RF) source is used to modulate the phase of the laser output via a phase modulator (PM). This phase modulation results in the creation of multiple sidebands, forming a comb-like spectrum of OFC lines.

In our proposed model, these initial OFC lines are further amplified using a single semiconductor optical amplifier (SOA). The purpose of the SOA is twofold: to increase the power of the generated OFC lines and to exploit the nonlinear properties of the SOA to generate additional lines through nonlinear interactions. Specifically, when a few OFC lines are launched into the SOA, nonlinear phenomena such as four-wave mixing occur, which effectively generate new frequency components, thereby increasing the total number of optical carriers available for subsequent processing.

Following the OFC generation, the WSS is employed to select specific wavelengths or sets of wavelengths from the comb spectrum. This selection process is critical for controlling the spectral components that will participate in the THz wave generation, ensuring that the desired spectral lines are transmitted to the next stage with appropriate power levels.

The selected optical signals are then modulated using in-phase and quadrature (IQ) modulators, which encode the information onto the optical carriers in a phase-coherent manner. These modulated signals are subsequently transmitted over the optical fiber and, after suitable processing, detected at the receiver end to recover the transmitted information and generate the THz signal.

The simulation was conducted using the virtual photonic integration (VPI) tool and MATLAB R2023a running on a computer Windows 11 64-bit equipped with Intel Core i7-12700K, 3.6 GHz, and memory specifications of 32 GB RAM. These specifications ensured sufficient computational resources for the simulations.

As depicted in Figure 2, the initial stage features a single CW laser source operating at 193.1 THz (1552.52 nm) with a linewidth of 100 kHz, alongside a sinusoidal RF signal at 12.5 GHz. Both the CW and RF signals are modulated using the PM, and the resulting output spectrum is presented in Figure 3. In this figure (blue), we observe that the generated OFC lines have a spacing of 12.5 GHz, resulting in a total of 24 lines.

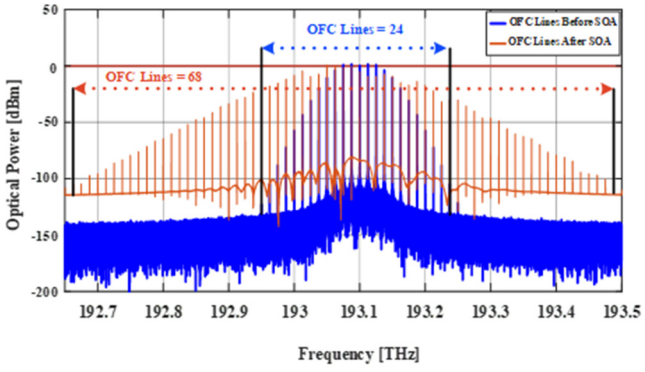


Figure 3. Optical spectrum of the generated comb lines: with SOA (red) and without SOA (blue).

Subsequently, these OFC lines are fed into the SOA, where its nonlinear effects are harnessed to produce a greater number of OFC lines, thereby expanding the THz range. As shown in Figure 3 (red), the number of OFC lines obtained after incorporating the SOA rises to 68, approximately three times the amount without the SOA. This increase is attributed to the SOA operating in deep saturation, utilizing its nonlinear FWM-induced carrier density modulation (CDM) properties.

FWM is a third-order nonlinear optical phenomenon that occurs when multiple optical waves interact in a nonlinear medium, generating new frequency components. It is a parametric process, meaning it does not involve energy exchange with the medium (i.e., no net energy is absorbed by the material). In this paper we utilized the FWM phenomenon to enhance the number of injected carriers into the SOA and establish phase correlation among all the comb lines.

In the next stage, we need to select the two required optical frequency comb lines by the WSS, so the output optical spectrum of WSS will include two optical carriers with separation of $(n_1 - n_2) \times f_{rf}$. Where f_{rf} is the radio frequency of the RF source, n_1 and n_2 are the first and second selected carrier, respectively. For example, in our case, we selected $(n_1 = 4)$, $(n_2 = -4)$, and $f_{rf} = 12.5$ GHz, so the optical carrier separation will be (8×12.5 GHz = 100 GHz = 0.1 THz). The first wavelength selected by WSS acts as an optical local oscillator (LO) at −4th order of OFC lines (at 193.05 THz), and the other is at +4th order of OFC lines, which is carrying a 4 Gbps QPSK baseband modulation signal, as shown in Figure 4.

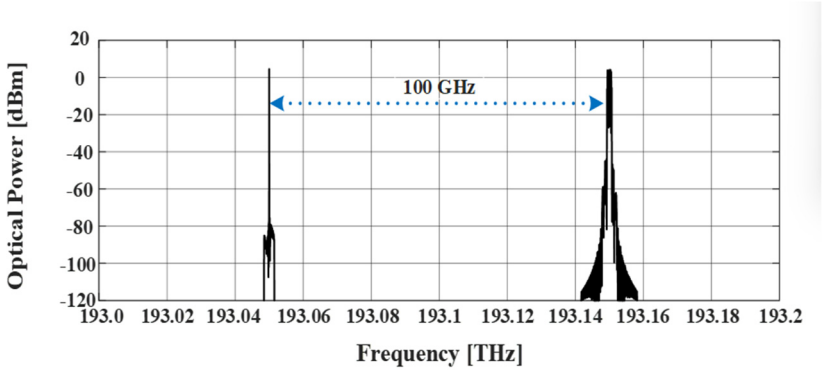


Figure 4. Optical spectrum before UTC-PD.

On the receiver side, the two optical carriers are combined and passed through a variable optical attenuator (VOA). This step allows for the precise control of the signal's power level to optimize the performance of the subsequent components. The combined signal is then directed to a UTC-PD, which is a highly efficient photodetector with a responsivity of 1 A/W, indicating that it generates 1 ampere of current for every watt of optical power it receives.

Within the UTC-PD, the two optical carriers interfere with each other. This interference results in the generation of a photonic vector THz-wave signal, characterized by a center frequency of 0.1 THz. The process of interference within the UTC-PD is crucial as it converts the optical signals into a terahertz signal, which is essential for high-frequency wireless communication applications. The generated THz signal is modulated using QPSK, a modulation scheme that allows the transmission of two bits per symbol, thereby increasing the data rate.

The input optical power to the UTC-PD is maintained at −4 dBm, a level chosen to ensure optimal performance and to avoid any potential issues, such as signal distortion or excessive noise.

This entire process is comprehensively illustrated in Figure 5, which offers a detailed visual representation of the signal flow and the interactions among various components within the system. The figure depicts how the optical carriers generated from the laser sources are first combined using a beam combiner, forming a composite optical signal that contains the necessary information for subsequent processing. This combined optical signal then passes through a variable optical attenuator (VOA), which allows for precise control of the optical power level, ensuring optimal conditions for detection and modulation.

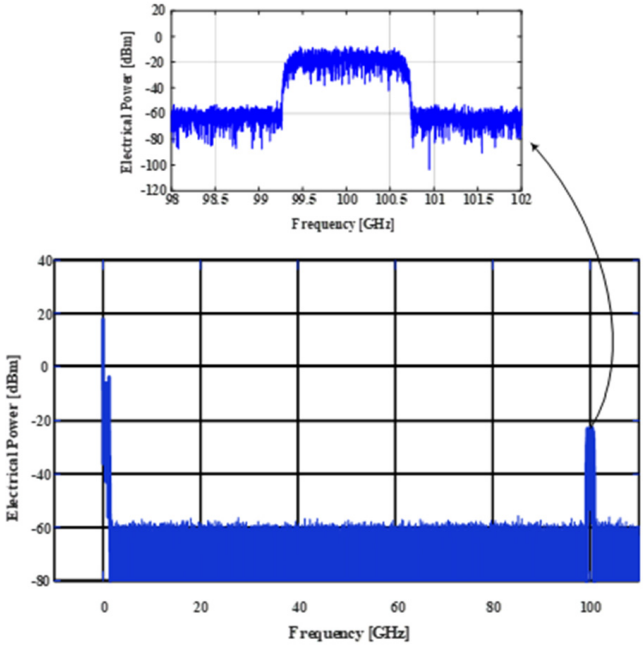


Figure 5. Electrical RF spectrum after PD of generated THz signal at 100 GHz.

Following this, the attenuated optical signal is directed onto the UTC-PD, a high-speed photodetector that converts the optical signal into a corresponding electrical signal. The UTC-PD's role is critical in generating a high-frequency electrical signal that embodies the modulated information, in this case, QPSK modulation, which is essential for high-capacity THz communication. The figure also highlights the key components involved in this conversion process, including the optical couplers, the VOA, and the photodiode, along with the signal pathways connecting them.

Once the electrical THz signal is generated, it is transmitted to the subsequent detection and demodulation stages, which are also represented in the diagram. The visual layout clarifies the sequence of operations on the receiver side, illustrating how the optical input is transformed into a modulated THz carrier and subsequently processed for data retrieval. Overall, Figure 5 provides an intuitive and detailed overview of the entire receiver architecture, emphasizing the flow of the optical and electrical signals, the role of each component, and the operational steps necessary to realize the THz communication system with QPSK modulation.

Following this, the generated photonic THz signal is amplified using an electrical amplifier equipped with a Bessel bandpass filter that has a center frequency of 0.1 THz and a bandwidth of 1.5 GHz, achieving a transmission gain of 35 dB. A 0.1THz local oscillator (LO) signal is then employed for coherent demodulation.

Ultimately, the transmitted data is extracted from the 0.1 THz RF signal utilizing digital signal processing (DSP) algorithms, which include the cascaded multi-modulus algorithm (CMMA), frequency down conversion, equalization, dispersion compensation, phase offset estimation, frequency offset estimation (FOE), and bit error rate (BER) calculation. The key parameters of the proposed system are summarized in Table 2.

In communication systems, modulation plays a vital role in the effective transmission of information. The choice of modulation scheme involves balancing various factors, including cost, complexity, radio frequency (RF) channel characteristics, component technologies, and noise levels. Given that THz frequency bands are not yet widely utilized, the design process faces technical challenges, such as significant channel losses, power management, and oscillator phase stability. Therefore, selecting an appropriate modulation scheme for THz communication systems is essential. This work explores several modulation formats,

including QPSK, 16-QAM, 64-QAM, and 256-QAM, within the THz generation context, and examines how different modulation orders influence the resulting THz signal. Figure 6 illustrates the relationship between bit error rate (BER) and received optical power. The results show that for QAM signals, the performance was very poor. Hence, using QPSK is a recommended choice for these applications.

Table 2. Simulation parameters' values.

Modulation Parameters	Value
Modulation order	QPSK
RF carrier frequency	12.5 GHz
RF amplitude	1 a.u
Signal data rate	4 Gbps
CW laser 1 frequency	193.1 THz
CW laser 1 power	1 mW
CW laser 1 linewidth	100 kHz
SRRC roll-off factor	0.18
Responsivity of PD	1 A/W
Thermal noise	10×10^{-12} A/Hz$^{(1/2)}$
SOA's Parameters	
Injection current (IC)	0.25 A
Height	80 µm
Length	500 µm
Width	3 µm
Optical confinement factor	0.99
Index to gain coupler	3.8
Waveguide loss coefficient	4000 1/m
DD-MZM's Parameters	
Extinction ratio	35 dB
$V_P DC V_P RF$	0.5 V 0.5 V
Insertion loss	6 dB
Operation temperature	25 degC
Extinction ratio	35 dB

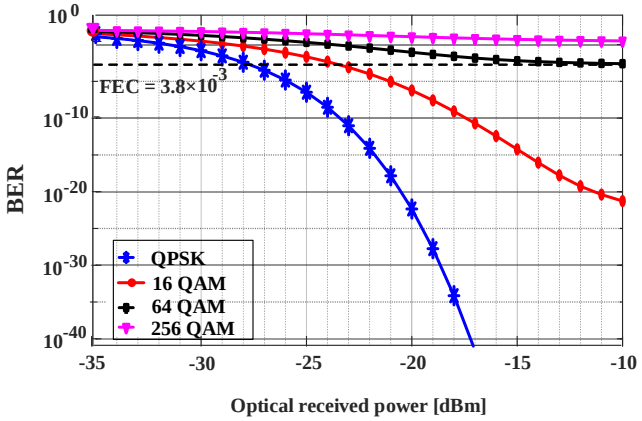


Figure 6. BER measurements versus optical power for different types of modulation orders.

As observed, our current implementation reliably supports only QPSK, with BER exceeding acceptable thresholds (>10^{-3}) for 16/64/256-QAM under tested channel conditions—primarily due to phase noise sensitivity from low-cost oscillators at higher symbol rates, nonlinear distortion in the power amplifier degrading EVM, and channel es-

timation errors under high Doppler spread. To evolve toward 6G's high-capacity demands, we propose future enhancements, including: advanced DSP using neural-network-based equalizers to compensate nonlinearities/phase noise; hybrid ARQ combined with LDPC coding for robust 256-QAM; hardware upgrades integrating GaN-based PAs and high-resolution ADCs to improve SNR by >6 dB; and multi-antenna MIMO techniques to mitigate fading. These steps align with 3GPP's 6G study items (e.g., AI-native air interfaces and sub-THz support), enabling our platform to scale beyond 100 Gbps. We will incorporate these solutions in the next hardware revision and validate them against 3GPP Rel-21 requirements.

In 6G communications, which aim for ultra-high data rates, extremely low latency, high spectral efficiency, and reliable connectivity, the performance metrics such as BER and EVM are critical indicators of the system's capability to meet these demanding requirements. The correlation with practical applications:

Quality of Service (QoS): Low BER and EVM values are necessary to guarantee QoS in applications like remote surgery, holographic communications, or autonomous driving, where errors can have critical consequences.

Spectral Efficiency: High-order modulation schemes used in 6G require precise signal quality; thus, low EVM is crucial to prevent error propagation and to maximize data throughput.

Robustness and Reliability: Maintaining these metrics within acceptable thresholds ensures the system can operate reliably under varying channel conditions, multipath effects, and interference, which are common in real-world environments.

Energy Efficiency: Systems with low BER and EVM reduce the need for retransmissions and complex error correction, saving power a vital aspect for battery-powered IoT devices and mobile terminals.

Achieving low BER and EVM directly supports the core objectives of 6G—high reliability, efficiency, and low latency—making these metrics not just performance indicators but essential parameters for ensuring that the communication system can meet the stringent demands of next-generation applications.

In the stage of measuring the performance of the generated THz signal, we simulated the bit error rate (BER), which refers to comparing the recovered data from the received signal to the original transmitted data. The BER for the generated optical vector THz signal as a function of optical received power is depicted in Figure 7a. The results show that the BER decreases as the optical received power increases. At the HD-FEC threshold value of 3.8×10^{-3}, the corresponding optical received power is -16.5 dBm.

Subsequently, we included the error vector magnitude (EVM) metric in our performance assessment, as it serves as an important measure of the radio transmitter or receiver's performance in digital communications.

We analyzed the EVM in relation to the optical received power for the generated optical vector THz signal, with the findings presented in Figure 7b. The EVM decreases with increasing optical received power. At the EVM threshold value of 5.6%, as noted in [62], the power level is approximately -13 dBm. Additionally, the constellation diagram is distinctly separated and clearly defined.

In the subsequent analysis, we examined the bit error rate (BER) under two scenarios: back-to-back (BtB) transmission and transmission over a 15 km SMF, as illustrated in Figure 8. The results indicate that the BER decreases as the optical received power increases for both the BtB and SMF cases. At the HD-FEC threshold value of 3.8×10^{-3}, the power for BtB transmission is -16.7 dBm, while for the 15 km SMF transmission, it is -15.2 dBm. This results in a power penalty of 1.5 dB between the two scenarios, attributed to fiber dispersion and phase fluctuations. Nevertheless, this difference can be considered negligible, and we

can treat the SMF at this length as effectively transparent, as will be demonstrated in the experimental results.

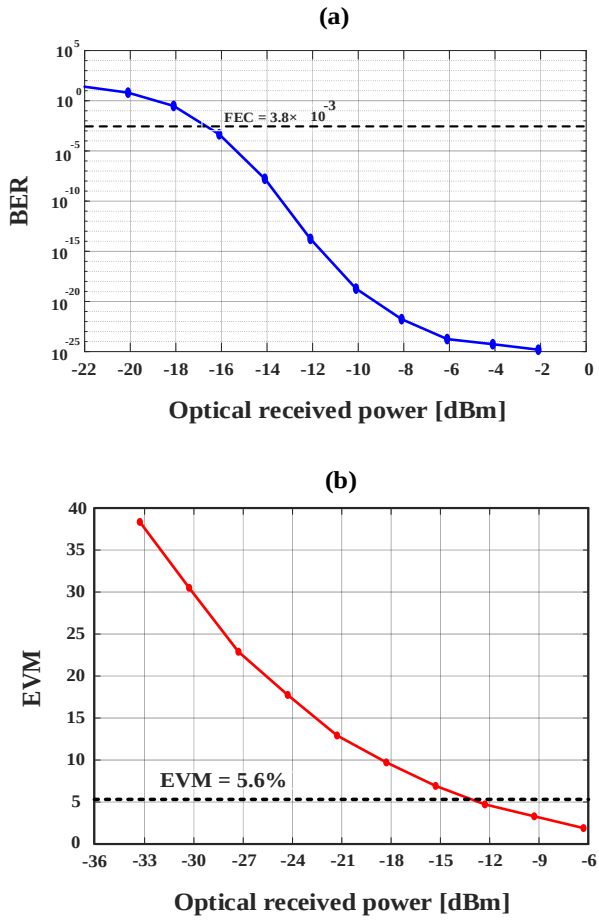


Figure 7. Performance curves for generated vector THz-wave signal for (**a**) BER and (**b**) EVM versus optical received power.

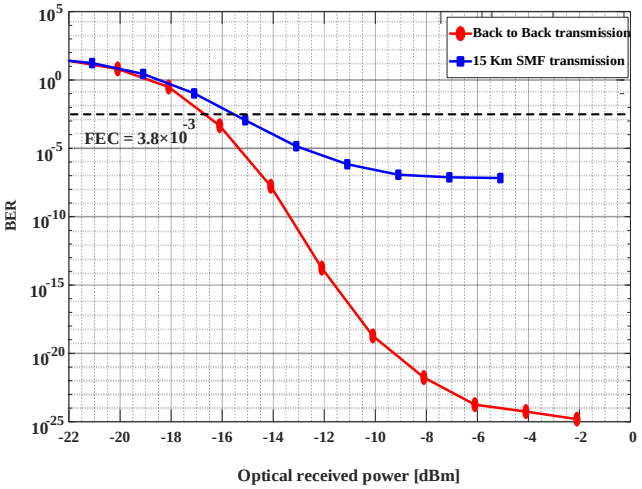


Figure 8. BER curves for BtB transmission and SMF 15 km.

Upon analyzing Figures 7 and 8 alongside the findings presented in reference [58], it becomes evident that there has been a notable enhancement in power performance. This comparison not only highlights the advancements achieved but also underscores the effectiveness of the methodologies employed in the current study. The improvements observed suggest a shift in power efficiency, indicating that the new approaches may

lead to more robust applications in the field. As we delve deeper into the data, it is clear that these enhancements could have far-reaching implications for future research and practical implementations.

3. Experimental Setup for THZ Signal Generation

The experimental setup for the photonic THz generation technique is depicted in Figure 9. The initial stage focuses on the generation of an OFC, with a SOA as the primary component to produce additional OFC lines. A low-noise single-frequency continuous wave (CW) laser diode operates at a wavelength of 1552.52 nm (193.1 THz) with an output power of 16 dBm and a linewidth of 100 kHz. This laser is connected to a phase modulator (PM) from Eospace, which is driven by a 12.5 GHz RF signal generated by a vector signal generator (VSG) with 11.3 dBm output power. The output spectrum of the optical signal before and after modulation are illustrated in Figures 10a and 10b, respectively.

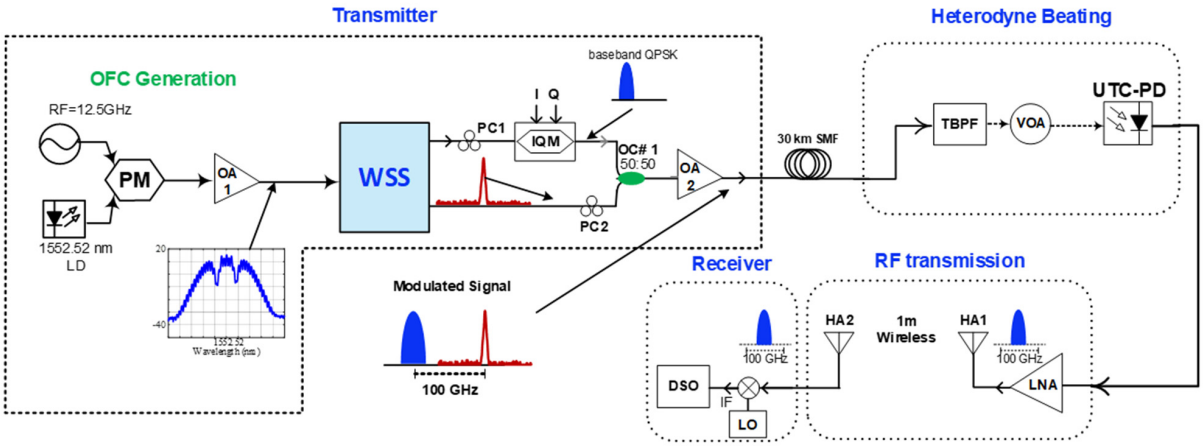


Figure 9. Experimental photonic setup for THz signal generation.

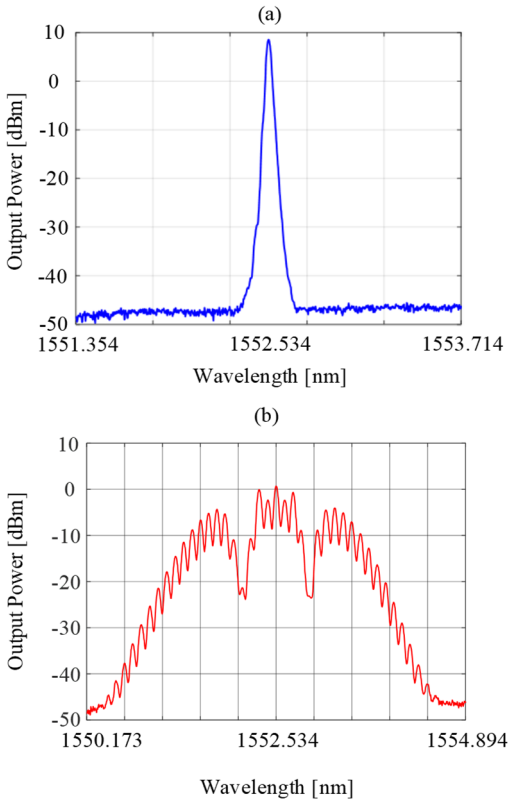


Figure 10. Output spectrum (**a**) before PM and (**b**) after PM.

The non-ideal behaviors of SOA, particularly ASE noise and gain recovery dynamics, significantly influence system performance. The ASE noise generated within the SOA is a critical factor, with the noise figure (NF) typically ranging between 5–7 dB, representing the excess noise added by the amplifier. This elevated ASE noise directly contributes to increased phase noise and amplitude fluctuations in the optical signal, which deteriorate the signal-to-noise ratio. Consequently, these effects impair phase coherence and cause uneven flatness across the comb spectrum, leading to higher bit error rates (BER) and increased error vector magnitude (EVM).

Additionally, the carrier lifetime (τc) and gain recovery time (τg) are vital parameters that determine the dynamic response of the SOA. Usually spanning hundreds of picoseconds to nanoseconds, the carrier lifetime influences how quickly the gain can respond to input power fluctuations. The gain recovery time indicates how long it takes for the gain to stabilize after saturation; shorter recovery times enable better handling of high-speed modulation but may induce gain fluctuations. For example, a carrier lifetime of around 300 ps and a gain recovery time near 1 ns can lead to gain saturation effects during high modulation rates, causing amplitude and phase distortions. These gain dynamics introduce amplitude modulation (AM) to phase modulation (PM) conversion, resulting in phase noise and reduced phase coherence among the comb lines. Moreover, gain fluctuations can cause spectral non-uniformity, affecting the flatness of the comb spectrum [63].

The combined effects of ASE noise and gain dynamics also impact the uniformity and coherence of the comb lines. Variations in ASE noise and gain behavior can cause amplitude deviations exceeding 1–2 dB across the spectrum, compromising line flatness. Simultaneously, gain fluctuations and ASE-induced phase noise introduce phase jitter, which reduces mutual coherence between lines. This can be characterized via phase noise spectral density or linewidth measurements, illustrating the degradation in phase coherence. These impairments translate into increased BER, especially in higher-order modulation schemes, where phase and amplitude noise elevate the likelihood of symbol errors often resulting in BER degradations of 10^{-3} or more. Similarly, EVM, which quantifies the deviation of the received signal from the ideal constellation, increases with these instabilities, with values exceeding 10–15% indicating significant impairment due to SOA non-idealities [64].

In summary, the ASE noise characterized by the noise figure and the gain recovery dynamics governed by carrier lifetime and recovery times significantly shape the spectral and temporal qualities of optical combs. A thorough quantitative understanding of these factors enables system designers to optimize SOA biasing, implement noise filtering, and apply advanced signal processing techniques to mitigate their adverse effects, thereby improving comb flatness, phase coherence, BER, and EVM in practical systems.

The output of the PM is fed into two types of SOAs: the Kamelian SOA (with an input power of 3.47 dBm and an output power of 14 dBm) and the Amonics SOA (with an input power of 3.47 dBm and an output power of 14.4 dBm). Both SOAs yielded similar results, showing no significant change in the number of generated OFC lines, as illustrated in Figure 11a,b.

When compared to the simulation results presented in Figure 3, the SOAs used in the lab have specific parameters that cannot be modified, including dimensions, optical confinement factors, insertion losses, and the index of gain couplers. The only adjustable parameter is the injection current for the SOAs, which is set at 0.25 A for the VPI SOA, 0.225 A for the Kamelian SOA, and 0.4 A for the Amonics SOA.

The output of the OFC is first amplified using Amonics AEDFA and then directed to the WSS to isolate two primary carriers spaced 0.1 THz apart. One carrier operates at baseband without modulation, exhibiting a power level of -4.1 dBm, while the second carrier, with a power level of -5.1 dBm, is modulated using an IQ modulator. The modulated carrier

supports data rates of 4 Gbps for QPSK, and is subsequently amplified with an EDFA. The input and output signals of the WSS are illustrated in Figure 12.

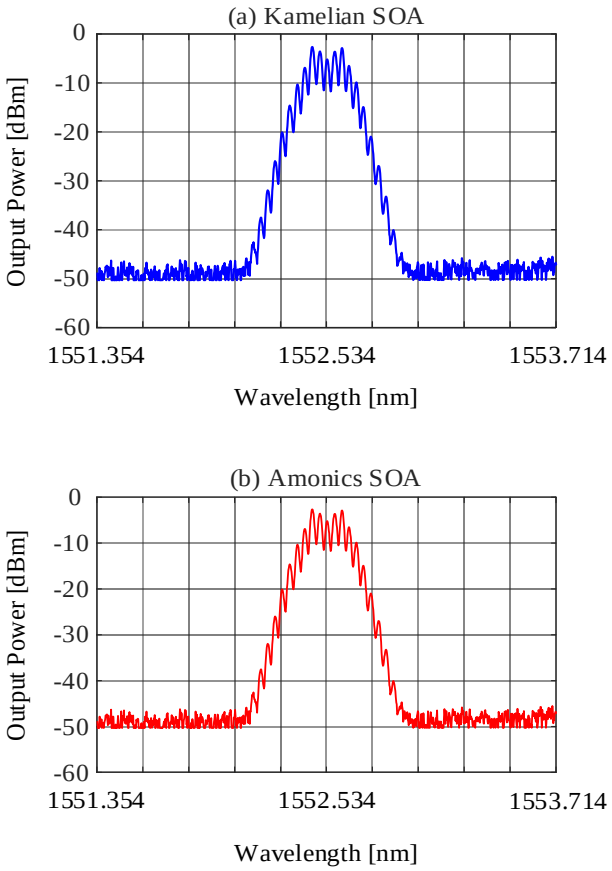


Figure 11. Optical frequency comb lines after (**a**) Kamelian SOA and (**b**) Amonics SOA.

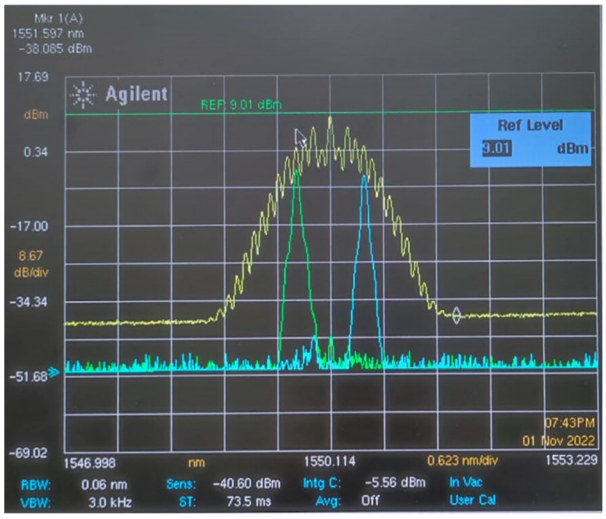


Figure 12. Optical spectrum of WSS input and output.

Subsequently, the two carriers, one modulated and the other unmodulated, are combined using a 50:50 optical coupler and directed into a photodiode (PD) with an input power of −6.4 dBm.

This photodiode has a responsivity of 0.6 A/W allowing us to obtain the electrical 0.1 THz signal. However, due to hardware limitations, the analyzer is unable to display the electrical signal in the 0.1 THz range. Specifically, since the oscilloscope used has

a 32 GHz bandwidth and cannot directly measure the 0.1 THz signals, we employed a heterodyne down-conversion technique. This involved mixing the high-frequency THz signal with a local oscillator (LO) signal to produce an intermediate frequency (IF) within the measurement bandwidth of the oscilloscope. The resulting lower-frequency signal could then be accurately captured and analyzed. Although we can assess the performance of the generated THz signal, as will be elaborated in the following sections.

The electrical signal is then fed into a low-noise amplifier, which is necessary because the signal transmitted over a 0.1THz RF link experiences significant power loss. The amplified signal is transmitted over a 1-m wireless channel using two horn antennas.

The THz signal is subsequently captured by a high-bandwidth digital storage oscilloscope, which features a bandwidth of 32 GHz and a sampling rate of 80-GSa/sec. The received signals undergo analysis using vector signal analyzer software VSA 21.2. Before demodulation, several digital signal processing (DSP) steps are performed, including signal down-conversion, carrier and clock recovery, baseband filtering with a root-raised cosine (RRC) filter with a roll-off factor of 0.35, and adaptive equalization to compensate for linear distortions.

The EVM analysis was conducted across three different scenarios to evaluate the system's performance under various transmission conditions. The first scenario involved a BtB configuration, serving as a baseline measurement where the signal is processed without any fiber transmission. Results from this scenario are presented in Figure 13, providing a reference for the system's optimal performance. It is observed that the EVM remains within acceptable limits up to a certain power level, with the forward error correction (FEC) threshold for QPSK modulation, typically around 37% rms as reported in [65,66], being reached at approximately -13.5 dBm. The constellation diagram accompanying this figure illustrates the quality of the received signal at this threshold, showing well-defined constellation points with minimal distortion, which indicates reliable demodulation and decoding.

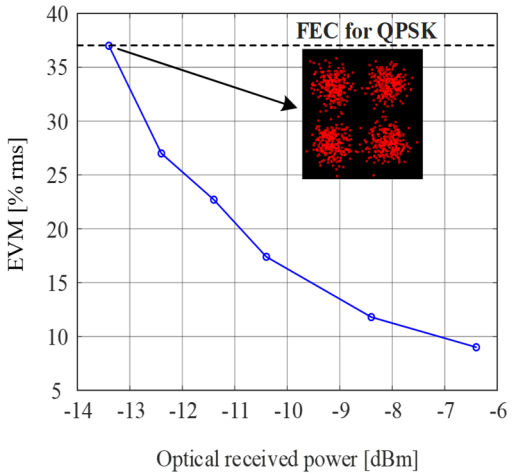


Figure 13. EVM versus optical received power for QPSK THz signal over BtB transmission.

The second scenario extends the transmission over 30 km of single-mode fiber (SMF), introducing realistic channel impairments, such as dispersion, attenuation, and potential nonlinear effects. Despite these challenges, the EVM results demonstrate that the system maintains acceptable performance levels, with only a marginal increase compared to the BtB case. This indicates the robustness of the proposed scheme over long-distance fiber links and underscores its potential for practical deployment in fiber-based THz communication systems.

The third scenario combines a short-range wireless link of 1 m with the 30 km fiber transmission, forming a hybrid wireless–fiber configuration. This setup aims to evaluate the system's capability to handle combined wireless and optical channel impairments, such as free-space path loss and fiber dispersion. Preliminary results suggest that while the EVM slightly increases in this hybrid scenario, it still remains within the acceptable limits for reliable QPSK demodulation. This hybrid approach demonstrates the flexibility of the system in supporting integrated wireless and fiber networks, which is a vital consideration for future high-capacity, flexible communication infrastructures.

Overall, these three scenarios comprehensively assess the system's resilience and performance under different transmission conditions, providing valuable insights into its suitability for real-world applications. Further analysis of the constellation diagrams and EVM trends across varying power levels and link configurations could offer deeper understanding of the system's limitations and optimization pathways.

It is important to note that the distance of the wireless channel is constrained by the limited space in the indoor laboratory.

The second scenario investigates the performance of the generated THz signal after transmission over a 30 km span of SMF, as illustrated in Figure 14. This assessment aims to evaluate the signal integrity and robustness in a realistic transmission environment, which is essential for practical communication systems. The results demonstrate that the transmitted signal experiences only a slight power penalty of approximately 0.3 dB compared to the BtB configuration, where no transmission loss occurs. This minimal power degradation suggests that the system retains high signal quality over extended fiber links, indicating effective preservation of the signal's amplitude and phase characteristics. Such a small power penalty is indicative of low insertion loss and minimal dispersion or nonlinear effects impacting the signal during propagation. Additionally, this finding highlights the potential for deploying this THz generation and transmission scheme in real-world fiber-optic networks, where maintaining signal strength and quality over long distances is critical. Further analysis of the received signal's spectral and phase stability post-transmission could provide deeper insights into the system's resilience, paving the way for practical high-capacity THz communication links in future wireless networks.

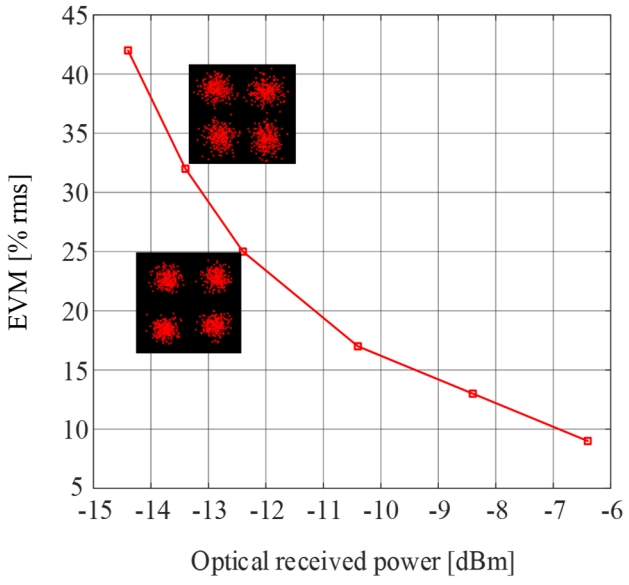


Figure 14. EVM versus optical received power for QPSK THz signal over 30 km SMF transmission.

Notably, at the QPSK threshold value of 37%, the received power registers at −13.8 dBm. These findings aligned with the results obtained in the simulation phase

(Figure 8), which also indicated that the power penalty between the BtB and SMF transmission is negligible.

The third scenario assesses the performance of the generated THz signal using a hybrid transmission that combines 30 km of SMF with a 1-m RF wireless channel. The results presented in Figure 15 indicate that the optical received power reaches −8.5 dBm at the QPSK threshold value of 37%. As seen from this Figure, the required power (−8.5 dBm) of 1 m RF channel transmission is high compared to BtB transmission (−13.8 dB) due to the losses in the wireless channel.

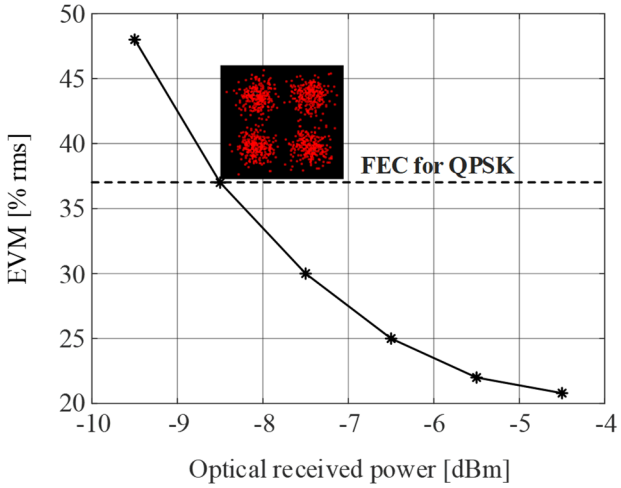


Figure 15. EVM versus optical received power for QPSK THz signal over hybrid transmission (30 km SMF and 1 m RF wireless channel).

Table 3 shows all the components used in the experimental section with the corresponding model.

Table 3. Components versus model.

Component	Model Number
Continuous wave (CW)	Koheras ADJUSTIK
Vector signal generator (VSG)	KEYSIGHT E8267D
Kamelian SOA	SOA-NL-L1-C-FA
Amonics SOA	SOA15-20-R
Amonics EDFA	EDFA-PA-40-B-FA
WSS	FINISAR WaveShaper 4000s 4903306
IQ modulator	FUJITSU 78110
Photodiode (PD)	FINISAR XPDV4121R 10 125 011 235130 B9W.0375
Analyzer	Infiniium DSO-X-93204A
Low-noise amplifier	QuinStar QLW-24403336-J0
Horn antennas	SAGE SAR-2507-28-S2
Digital storage oscilloscope	Keysight DSOX 932048
Vector signal analyzer software	Keysight VSA 89600

4. Conclusions

This paper presents a comprehensive study on the generation of a 0.1 THz photonic vector THz-wave signal utilizing a simple PM-based optical frequency comb and an IQ modulator for signal modulation, supported by experimental and simulation results from a photonic-based approach for THz signal generation in next-generation communication network applications. Through numerical simulations, we have demonstrated the feasibility of THz signal generation. The experimental setup, serving as a proof-of-concept, has

successfully generated and transmitted 4 Gbps QPSK signals at a frequency of 0.1 THz over a hybrid fiber/RF channel. The transmitted signal was received with BER and EVM below the FEC limit.

In our experimental setup, we successfully generated and transmitted a 4 Gbps QPSK photonic vector THz wave signal. The process begins with a phase modulator driven by a 12.5 GHz radio frequency signal to generate an optical frequency comb. This comb undergoes heterodyne mixing in UTC-PD, producing a 0.1 THz radio frequency signal. The THz signal is then transmitted over a 30 km span of single-mode fiber, operating in a hybrid mode. The resulting electrical 0.1 THz vector signal, modulated with QPSK, achieves a (BER below the threshold of 3.8×10^{-3} corresponding to the HD-FEC limit.

This study provides valuable insights for further research into high-frequency vector THz-wave signal generation, highlighting that advancements in related optical devices will significantly enhance the development of photonic THz-wave signal generation technology, promising a bright future for this field.

Author Contributions: Conceptualization, Y.A. and A.M.R.; Methodology, Y.A.; Software, A.M.R.; Validation, A.M.R., F.M.I. and S.A.A.; Formal analysis, Y.A.; Investigation, Y.A. and M.A.E.; Resources, A.M.R.; Writing—original draft, Y.A.; Writing—review & editing, Y.A., M.A.E. and S.A.A.; Supervision, A.M.R., S.M.I., F.M.I. and S.A.A.; Project administration, S.A.A.; Funding acquisition, M.A.E. All authors have read and agreed to the published version of the manuscript.

Funding: This work was supported by the Researchers Supporting Project, King Saud University, Riyadh, Saudi Arabia, under Grant RSP2025R46.

Data Availability Statement: The original contributions presented in this study are included in the article. Further inquiries can be directed to the corresponding author.

Conflicts of Interest: The authors declare no conflicts of interest.

References

1. Bhat, J.R.; Alqahtani, S.A. 6G ecosystem: Current status and future perspective. *IEEE Access* **2021**, *9*, 43134–43167. [CrossRef]
2. Ahad, A.; Jiangbina, Z.; Tahir, M.; Shayea, I.; Sheikh, M.A.; Rasheed, F. 6G and Intelligent Healthcare: Taxonomy, technologies, open issues and future research directions. *Internet Things* **2024**, *25*, 101068. [CrossRef]
3. Singh, A.; Andrello, M.; Thawdar, N.; Jornet, J.M. Design and operation of a graphene-based plasmonic nano-antenna array for communication in the terahertz band. *IEEE J. Sel. Areas Commun.* **2020**, *38*, 2104–2117. [CrossRef]
4. Ma, X.; Chen, Z.; Chen, W.; Li, Z.; Chi, Y.; Han, C.; Li, S. Joint channel estimation and data rate maximization for intelligent reflecting surface assisted terahertz MIMO communication systems. *IEEE Access* **2020**, *8*, 99565–99581. [CrossRef]
5. Pennanen, H.; Hänninen, T.; Tervo, O.; Tölli, A.; Latva-Aho, M. 6G: The Intelligent Network of Everything. *IEEE Access* **2024**, *13*, 1319–1421. [CrossRef]
6. Wei, H.; Ge, H.; Zhao, T.; Sharma, S.; Petru, M.; Dwivedi, S.P.; Kumar, A.; Abbas, M. Vanadium dioxide thin films-assisted terahertz meta-surface for simultaneous absorption, polarization conversion bi-functional switching, and wavefront operation. *Results Phys.* **2023**, *53*, 106970. [CrossRef]
7. Alkhlefat, Y.; Esmail, M.A.; Ragheb, A.M.; Idrus, S.M.; Iqbal, F.M.; Alshebeili, S.A. Experimental Investigation of All-Optical Sub-THz Wavelength Conversion for 6G Communication Systems. *IEEE Access* **2024**, *12*, 133521–133531. [CrossRef]
8. Yang, S.; Han, Q.; Sun, Z.; Wei, P.; Gao, C.; Zhang, Y.; Chen, Q.; Kang, J.; Wang, S.; Xiao, H.; et al. Stretchable, Transparent, and Ultra-Broadband Terahertz Shielding Thin Films Based on Wrinkled MXene Architectures. *Nano-Micro Lett.* **2024**, *16*, 165. [CrossRef]
9. Xu, R.; Gao, S.; Izquierdo, B.S.; Gu, C.; Reynaert, P.; Standaert, A.; Gibbons, G.J.; Bosch, W. A review of broadband low-cost and high-gain low-terahertz antennas for wireless communications applications. *IEEE Access* **2020**, *8*, 57615–57629. [CrossRef]
10. Sarieddeen, H.; Alouini, M.-S.; Al-Naffouri, T.Y. An overview of signal processing techniques for terahertz communications. *Proc. IEEE* **2021**, *109*, 1628–1665. [CrossRef]
11. Nagatsuma, T.; Ducournau, G.; Renaud, C.C. Advances in terahertz communications accelerated by photonics. *Nat. Photonics* **2016**, *10*, 371–379. [CrossRef]
12. Sengupta, K.; Nagatsuma, T.; Mittleman, D.M. Terahertz integrated electronic and hybrid electronic–photonic systems. *Nat. Electron.* **2018**, *1*, 622–635. [CrossRef]

13. Kenneth, O.; Choi, W.; Zhong, Q.; Sharma, N.; Zhang, Y.; Han, R.; Ahmad, Z.; Kim, D.Y.; Kshattry, S.; Medvedev, I.R.; et al. Opening terahertz for everyday applications. *IEEE Commun. Mag.* **2019**, *57*, 70–76.
14. Sengupta, K. Universal Terahertz Integrated Systems: Bridging the 'THz' and 'Application' Gap in the Next Decade. In Proceedings of the 2019 IEEE MTT-S International Microwave and RF Conference (IMARC), Mumbai, India, 13–15 December 2019; pp. 1–3.
15. Hussain, M.; Awan, W.A.; Alzaidi, M.S.; Hussain, N.; Ali, E.M.; Falcone, F. Metamaterials and their application in the performance enhancement of reconfigurable antennas: A review. *Micromachines* **2023**, *14*, 349. [CrossRef]
16. Hussain, M.; Zahra, H.; Abbas, S.M.; Zhu, Y. Flexible dielectric materials: Potential and applications in antennas and RF sensors. *Adv. Electron. Mater.* **2024**, *10*, 2400240. [CrossRef]
17. Wu, D.; Ma, Y.; Sun, Y.; Huang, R.; Zhang, J.; Liu, S.; Zhuo, N.; Zhai, S.; Cheng, F.; Liu, F.; et al. Monolithic dispersion engineered mid-infrared quantum cascade laser frequency comb. *Photonics Res.* **2024**, *12*, 2566–2572. [CrossRef]
18. Makhlouf, S.; Cojocari, O.; Hofmann, M.; Nagatsuma, T.; Preu, S.; Weimann, N.; Hübers, H.-W.; Stöhr, A. Terahertz sources and receivers: From the past to the future. *IEEE J. Microw.* **2023**, *3*, 894–912. [CrossRef]
19. Huang, S.-W.; Yang, J.; Yang, S.-H.; Yu, M.; Kwong, D.-L.; Zelevinsky, T.; Jarrahi, M.; Wong, C.W. Globally stable microresonator Turing pattern formation for coherent high-power THz radiation on-chip. *Phys. Rev. X* **2017**, *7*, 041002. [CrossRef]
20. Zhai, K.; Zhang, X.; Wang, W.; Chen, B.; Jin, Y.; Du, X.; Liu, Y.; Cui, J.; Li, Q.; Zhou, H.; et al. Photonic-Assisted Microwave Harmonic Down-Conversion Based on Four-Wave Mixing in a Silicon Integrated Waveguide Doped with Reverse-Biased P-i-N Junction. *J. Light. Technol.* **2023**, *41*, 7268–7275. [CrossRef]
21. Wang, W.; Tan, Y.J.; Tan, T.C.; Kumar, A.; Pitchappa, P.; Szriftgiser, P.; Ducournau, G.; Singh, R. On-chip topological beamformer for multi-link terahertz 6G to XG wireless. *Nature* **2024**, *632*, 522–527. [CrossRef]
22. Laube, S.M.; Gasser, C.; Schneider-Hornstein, K.; Zimmermann, H. Highly-Sensitive Integrating Optical Receiver with Large PIN Photodiode. *IEEE Photonics J.* **2024**, *16*, 7101809. [CrossRef]
23. Tian, Y.; Li, Y.; Dong, B.; Xiong, B.; Zhang, J.; Sun, C.; Hao, Z.; Wang, J.; Wang, L.; Han, Y.; et al. High-power MUTC Photodiode Module for Photonics-assisted Beyond 100 Gb/s Wireless Sub-THz Communications in the F-band. *J. Light. Technol.* **2024**, *42*, 5616–5623. [CrossRef]
24. Che, M.; Kondo, K.; Kato, K. Generating and enhancing THz pulses via an antenna-coupled unitraveling-carrier photodiode array. *IEEE Trans. Terahertz Sci. Technol.* **2023**, *13*, 280–285. [CrossRef]
25. Shi, J.-W. Ultra-Fast Photodiodes under Zero-and Forward-Bias Operations. In *Sensors for Diagnostics and Monitoring*; CRC Press: Boca Raton, FL, USA, 2018; pp. 65–96.
26. Chen, Q.; Zhang, X.; Sharawi, M.S.; Kashyap, R.; High, A.I. High–Power Photodiodes: From Fundamentals to Applications. *Appl. Sci.* **2024**, *14*, 3410. [CrossRef]
27. Ishibashi, T.; Shimizu, N.; Kodama, S.; Ito, H.; Nagatsuma, T.; Furuta, T. Uni-traveling-Carrier Photodiodes. In *Ultrafast Electronics and Optoelectronics*; Optica Publishing Group: Washington, DC, USA, 1997.
28. Ito, H.; Nakajima, F.; Furuta, T.; Yoshino, K.; Hirota, Y.; Ishibashi, T. Photonic terahertz-wave generation using antenna-integrated uni-travelling-carrier photodiode. *Electron. Lett.* **2003**, *39*, 1828–1829. [CrossRef]
29. Shehata, M.; Wang, Y.; He, J.; Kandeepan, S.; Wang, K. Optical and Terahertz Wireless Technologies: The Race to 6G Communications. *IEEE Wirel. Commun.* **2023**, *30*, 10–18. [CrossRef]
30. Renaud, C.C.; Robertson, M.; Rogers, D.; Firth, R.; Cannard, P.J.; Moore, R.; Seeds, A.J.; Jäger, D.; Stöhr, A. A High Responsivity, Broadband Waveguide Uni-Travelling Carrier Photodiode. In *Millimeter-Wave and Terahertz Photonics*; SPIE: Bellingham, WA, USA, 2006; Volume 6194, pp. 87–94.
31. Yu, X.; Jia, S.; Hu, H.; Galili, M.; Morioka, T.; Jepsen, P.U.; Oxenløwe, L.K. 160 Gbit/s photonics wireless transmission in the 300–500 GHz band. *Apl. Photonics* **2016**, *1*, 081301. [CrossRef]
32. Ullah, R.; Bo, L.; Ullah, S.; Mao, Y.; Feng, T.; Xin, X. Cost effective OLT designed from optical frequency comb generator based EML for1. 22 Tbps wavelength division multiplexed passive optical network. *Opt. Fiber Technol.* **2018**, *43*, 49–56. [CrossRef]
33. He, J.; Long, F.; Deng, R.; Shi, J.; Dai, M.; Chen, L. Flexible multiband OFDM ultra-wideband services based on optical frequency combs. *J. Opt. Commun. Netw.* **2017**, *9*, 393–400. [CrossRef]
34. Singh, N.; Bansal, B.N. An ultra-dense spacing-based PON by incorporating dual drive Mach–Zehnder modulator for comb generation. *J. Opt. Commun.* **2024**, *44*, s359–s365. [CrossRef]
35. Verma, P.; Singh, S. An approach to generate cross-polarization modulation-enabled optical frequency comb with enhanced spectral flatness in traveling-wave semiconductor optical amplifiers. *J. Opt.* **2024**, *26*, 105703. [CrossRef]
36. Ullah, R.; Ullah, S.; Chen, S.; Almadhor, A.; Al-Atawi, A.A.; Jianxin, R.; Khan, M.; Pau, G. 1.12 Tbps-16QAM Uncompensated LongHaul Transmission Employing a new SelfOscillating Optical Frequency Comb Generator both at transmitter and receiver. *IEEE Photonics J.* **2024**, *16*, 7200507. [CrossRef]

37. Yang, W.Y.; Jiang, Z.F.; Cui, B.; Jin, Y.H. Generation of Wideband Optical Frequency Comb with Coincident Polarization Based on Gain-Switched Vertical-Cavity Surface-Emitting Laser under Orthogonal Optical Injection. *IEEE Access* **2024**, *12*, 181454–181461. [CrossRef]
38. Zhang, S.; Wang, Z.; Zuo, X.; Ma, C.; Jiang, Y.; Yu, J. Generation of a Flat Optical Frequency Comb via a Cascaded Dual-Parallel Mach–Zehnder Modulator and Phase Modulator without Using the Fundamental Tone. *Photonics* **2023**, *10*, 1340. [CrossRef]
39. Sohanpal, R.S. Optical Frequency Comb Generation and Applications in Coherent Optical Communications. Master's Thesis, University College London, London, UK, 2024.
40. Verma, P.; Singh, S. Exploiting cross-polarization modulation in semiconductor optical amplifier-Mach-Zehnder interferometer for enhanced optical frequency comb generation. *Opt. Eng.* **2024**, *63*, 115101. [CrossRef]
41. Ullah, S.; Ullah, R.; Zhang, Q.; Khalid, H.A.; Memon, K.A.; Khan, A.; Tian, F.; Xiangjun, X. Ultra-wide and flattened optical frequency comb generation based on cascaded phase modulator and LiNbO3-MZM offering terahertz bandwidth. *IEEE Access* **2020**, *8*, 76692–76699. [CrossRef]
42. Shen, J.; Wu, S.; Li, D. Ultra-flat optical frequency comb generation based on phase modulation with simple digital driving signal. *Optik* **2019**, *198*, 163254. [CrossRef]
43. Liu, Y.; Wu, S. Proposed Scheme for Ultra-Flat Optical Frequency Comb Generation Based on Dual-Drive Mach–Zehnder Modulators and Bidirectional Recirculating Frequency Shifting in Single Loop. *Photonics* **2022**, *9*, 514. [CrossRef]
44. Cui, Y.; Wang, Z.; Zuo, X.; Xu, Y.; Jiang, Y.; Yu, J.; Huang, Z. Flat optical frequency comb generation by using one DPMZM and superposed harmonics. *Opt. Commun.* **2023**, *531*, 129223. [CrossRef]
45. Qiu, J.; Jin, X.; Yang, L.; Xu, Y.; Wei, B. Generation of a 25-line flattened optical frequency comb and its coherent beating properties. *Appl. Opt.* **2022**, *61*, 3871–3876. [CrossRef]
46. Cui, Y.; Wang, Z.; Xu, Y.; Jiang, Y.; Yu, J.; Huang, Z. Generation of flat optical frequency comb using cascaded PMs with combined harmonics. *IEEE Photonics Technol. Lett.* **2022**, *34*, 490–493. [CrossRef]
47. Sharma, V.; Singh, S. Development of frequency comb generation by spectral broadening of periodic optical pulses in semiconductor laser amplifiers. *J. Opt.* **2022**, *24*, 045701. [CrossRef]
48. Li, J.; Ma, H.; Li, Z.; Zhang, X. Optical frequency comb generation based on dual-polarization IQ modulator shared by two polarization-orthogonal recirculating frequency shifting loops. *IEEE Photonics J.* **2017**, *9*, 1–10. [CrossRef]
49. Ujjwal; Kumar, R. Optical Frequency Comb Generator Employing Two Cascaded Frequency Modulators and Mach–Zehnder Modulator. *Electronics* **2023**, *12*, 2762. [CrossRef]
50. Gao, T.; Zhang, Y.; Li, J.; Li, S.; Zhang, Z.; Zhang, S.; Liu, Y. Tunable microwave frequency comb generation via periodic relaxation oscillation in directly modulated laser. *Opt. Laser Technol.* **2024**, *170*, 110295. [CrossRef]
51. Wang, X.; Li, Z.; Lyu, W.; Lyu, Y.; Zeng, C.; Zhang, Z.; Zhang, S.; Zhang, Y.; Li, H.; Xia, J.; et al. Flat optical frequency comb generation based on monolithic integrated LNOI intensity and phase modulator. *Photonics* **2022**, *9*, 495. [CrossRef]
52. Fang, X.; Lai, Z.; Guo, P.; Geng, J.; Zhang, Z. Large-Bandwidth Optical Frequency Comb Generator Based on Dual-Parallel Mach-Zehnder and Cascaded Intensity Modulators. *SSRN* **2023**, SSRN:4395465.
53. Xu, M.; He, M.; Zhu, Y.; Yu, S.; Cai, X. Flat optical frequency comb generator based on integrated lithium niobate modulators. *J. Light. Technol.* **2022**, *40*, 339–345. [CrossRef]
54. Lv, X.; Liu, J.; Wu, S. Flat optical frequency comb generation based on polarization modulator with RF frequency multiplication circuit and dual-parallel Mach-Zehnder modulator. *Optik* **2019**, *183*, 706–712. [CrossRef]
55. Sharma, V.; Singh, S.; Lovkesh. Cross-phase modulation based ultra-flat 90-line optical frequency comb generation. *Opt. Quantum Electron.* **2021**, *53*, 1–12. [CrossRef]
56. Zhang, X.; Zhao, L.; Zhang, J.; Zhang, J.; Zhang, Z.; Shen, M.; Chen, S.; Zheng, X.; Jiang, T. LSTM-Resnet-assisted Linearization for the Dual Frequency Comb Photonic RF Channelized Receiver. *J. Light. Technol.* **2024**, *42*, 7725–7735. [CrossRef]
57. Hasanuzzaman, G.; Shams, H.; Renaud, C.C.; Mitchell, J.; Seeds, A.J.; Iezekiel, S. Tunable THz signal generation and radio-over-fiber link based on an optoelectronic oscillator-driven optical frequency comb. *J. Light. Technol.* **2019**, *38*, 5240–5247. [CrossRef]
58. Yu, J.; Li, K.; Chen, Y.; Zhao, L.; Huang, Y.; Li, Y.; Ma, J.; Shan, F. Terahertz-wave generation based on optical frequency comb and single Mach-Zehnder modulator. *IEEE Photonics J.* **2020**, *12*, 1–8. [CrossRef]
59. Ding, Y.-Y.; Gao, F.; Yuan, H.-H.; Lv, Z.-R.; Yang, T. 1–2.9-Thz tunable terahertz beat signal generation based on inas/inp quantum-dot mode-locked laser. *IEEE Photonics Technol. Lett.* **2018**, *30*, 1234–1237. [CrossRef]
60. Wang, H.; Lu, D.; Zhang, R.; Zhao, L. Photonic Terahertz Carrier Generation Using an Optical Feedback Mode-Lock Laser Diode. *IEEE Photonics J.* **2021**, *13*, 1–6. [CrossRef]
61. Jia, S.; Lo, M.-C.; Zhang, L.; Ozolins, O.; Udalcovs, A.; Kong, D.; Pang, X.; Yu, X.; Xiao, S.; Popov, S.; et al. Integrated Dual-DFB Laser for 408 GHz Carrier Generation Enabling 131 Gbit/s Wireless Transmission over 10.7 Meters. In Proceedings of the Optical Fiber Communication Conference, Washington, DC, USA, 3–7 March 2019. Paper Th1C.2.

62. Alkhlefat, Y.; Ragheb, A.M.; Esmail, M.A.; Alshebeili, S.A.; Seleem, H.E. Millimeter wave switching for single carrier and aggregated filter bank multi-carrier signals in radio over fiber networks. *Opt. Fiber Technol.* **2020**, *60*, 102335. [CrossRef]
63. Shi, B.; Calabretta, N.; Stabile, R. InP photonic integrated multi-layer neural networks: Architecture and performance analysis. *APL Photonics* **2022**, *7*, 010801. [CrossRef]
64. Bougaud, A.; Llopis, O.; Fernandez, A. A parametric study of a SOA based COEO for phase noise performance and reliable operation. *J. Light. Technol.* **2023**, *42*, 2245–2251. [CrossRef]
65. Ragheb, A.M.; Tareq, Q.; Esmail, M.A.; Alrabeiah, M.R.; Alshebeili, S.A.; Khan, M.Z. Enabling WiGig communications using quantum-dash laser source under smoky weather conditions. *IEEE Photonics J.* **2022**, *14*, 1–7. [CrossRef]
66. Shafik, R.A.; Rahman, M.S.; Islam, A.R. On the Extended Relationships among EVM, BER and SNR as Performance Metrics. In Proceedings of the 2006 International Conference on Electrical and Computer Engineering (ICECE), Dhaka, Bangladesh, 19–21 December 2006; pp. 408–411.

Disclaimer/Publisher's Note: The statements, opinions and data contained in all publications are solely those of the individual author(s) and contributor(s) and not of MDPI and/or the editor(s). MDPI and/or the editor(s) disclaim responsibility for any injury to people or property resulting from any ideas, methods, instructions or products referred to in the content.